PHYSICAL REVIEW B **95**, 094417 (2017)

Unveiling the role of Co-O-Mg bond in magnetic anisotropy of Pt/Co/MgO using atomically controlled deposition and *in situ* electrical measurement

Yumeng Yang,[1] Jiaren Yuan,[2,3] Long Qi,[1] Ying Wang,[1] Yanjun Xu,[1,4] Xiaowei Wang,[1] Yuanping Feng,[3]
Baoxi Xu,[4] Lei Shen,[5,*] and Yihong Wu[1,†]

[1]*Department of Electrical and Computer Engineering, National University of Singapore, 4 Engineering Drive 3, Singapore 117583, Singapore*
[2]*College of Science, Nanjing University of Aeronautics and Astronautics, Nanjing 210016, People's Republic of China*
[3]*Department of Physics, Centre for Advanced Two-dimensional Materials, National University of Singapore, Singapore 117542, Singapore*
[4]*Data Storage Institute, Agency for Science, Technology and Research (A*STAR), 2 Fusionopolis Way,*
08-01 Innovis, Singapore 138634, Singapore
[5]*Department of Mechanical Engineering, Engineering Science Programme, Faculty of Engineering,*
National University of Singapore, Singapore 117575, Singapore

(Received 13 December 2016; revised manuscript received 20 February 2017; published 13 March 2017)

Despite the crucial role of interfacial perpendicular magnetic anisotropy in a Co(Fe)/MgO-based magnetic tunnel junction, the underlying mechanism is still being debated. Here, we report an anatomical study of the oxygen and Mg effect on Pt/Co bilayers through repeated *in situ* anomalous Hall effect measurements, controlled oxygen exposure, and Mg deposition in an ultrahigh vacuum system. We found that chemisorbed oxygen not only quenches the effective magnetic moment of the Co surface layer, but also softens its magnetic anisotropy. However, a subsequent Mg dusting on the oxygen preexposed Pt/Co surface can recover the magnetic anisotropy. The *ab initio* calculations on the exchange splitting and orbital hybridization near the Fermi level give a clear physical explanation of the experimental observations. Our results suggest that the Co(Fe)-O-*M* bond plays a more important role than the widely perceived Co(Fe)-O bond does in realizing interfacial perpendicular magnetic anisotropy in Co(Fe)/MgO heterostructures.

DOI: 10.1103/PhysRevB.95.094417

I. INTRODUCTION

Perpendicular magnetic anisotropy (PMA) is of great importance in building spin-transfer-torque or spin-orbit-torque-based spintronic devices due to its reduced process variation and excellent down scaling capability [1,2]. One class of materials that simultaneously exhibits stable PMA, large tunneling magnetoresistance (TMR), and low switching current is the ferromagnetic (FM) transition-metal/oxide heterostructures, including CoFeB/MO$_x$ and Co(Fe)/MO$_x$ ($M =$ Mg, Al, etc.) [3,4]. Experimentally it has been well established that a large PMA [5–10] or TMR [11–14] can be obtained through optimized plasma (natural) oxidation [5,6,11–13], postannealing [9,10], or the combination of both processes [7,8,14]. Results from *ab initio* calculations [15–17] suggest that the PMA originates from strong hybridization between the (Co)Fe-3d and the O-2p orbitals at the (Co)Fe/oxide interface, which can penetrate into (Co)Fe for a few atomic layers. It was further pointed out that an abrupt interface with a Co(Fe)-O bond is more desirable for a sizable PMA than either the underoxidized interface with a Co(Fe)-M bond or the overoxidized one with a Co(Fe)-O-Co(Fe) bond. The importance of the Co(Fe)-O bond for obtaining the PMA has recently been confirmed experimentally in CoFeB-MgO magnetic tunnel junctions by directly imaging the atoms using advanced electron microscopy, wherein it was found that CoFe bonds atomically to MgO grains in an epitaxial manner by forming a Co(Fe)-O bond at the interfaces without the incorporation of Co(Fe) into MgO or vice versa [18]. In another attempt, a maximum magnetic anisotropy of ~60 meV was obtained by directly placing a single Co atom atop the O site of an MgO (100) surface [19]. Both findings provided direct microscopic evidence that the origin of PMA lies in an interfacial Co(Fe)-O bond. However, in all these studies the oxygen comes from the oxide instead of free oxygen atoms or molecules, and it thus remains unclear whether a Co(Fe)-O alone or a Co(Fe)-O-M bond plays a more important role in forming the PMA. In order to elucidate the respective roles of Co-O and Co-O-Mg bonds in forming the PMA, we systematically studied the oxygen and Mg effect on the anisotropy of Pt/Co bilayers using an ultrahigh vacuum (UHV) system with a base pressure of $<5 \times 10^{-9}$ mbar, which allows for performing *in situ* deposition of Co and Mg with atomic layer accuracy, controlled adsorption of oxygen, and the anomalous Hall effect (AHE) measurements without breaking the vacuum.

The experiment began with the deposition of a Pt underlayer which is used to induce PMA in the subsequently deposited Co. In order to study the respective roles of oxygen and Mg, we performed O exposure and Mg deposition in sequences between which electrical measurements were carried out. This is in contrast with previous studies in which O and Mg are deposited simultaneously in the form of MgO [9,20]. By gradually increasing the Co thicknesses (t_{Co}) in Pt/Co bilayers, we observed the onset of PMA at $t_{\mathrm{Co}} \approx 0.6$ nm, and spin reorientation transition (SRT) [21–23] beyond $t_{\mathrm{Co}} \approx 1.7$ nm in which the easy axis changes from the perpendicular to the in-plane direction. Depending on t_{Co}, the subsequent oxygen exposure has a different effect on the effective anisotropy: It softens the PMA at $t_{\mathrm{Co}} = 0.6$ and 0.8 nm, but it enhances the PMA at $t_{\mathrm{Co}} = 1.9$ nm. Both can be understood as mainly caused by the O adsorption induced decrease in the effective

---

[*] shenlei@nus.edu.sg
[†] elewuyh@nus.edu.sg

2469-9950/2017/95(9)/094417(8)

magnetic layer thickness of Co, which is different from the reported oxygen effect on PMA of Co(Fe) in Co(Fe)/MO_x heterostructures [6,7,18]. Further deposition of a Mg dusting layer on top of the oxygen preexposed Pt/Co surface recovers the PMA, whereas direct dusting of Mg on clean Pt/Co surface reduces the PMA. Using a*b initio* calculations, we found that upon O adsorption the reduction of exchange splitting by charge transfer quenches the moment of the topmost Co layer, whereas the subsequently adsorbed Mg adatoms recover the moment by transferring some electrons back to Co. The rebalancing of charge transfer recovers the PMA. Although the sample structure under investigation is not exactly the same as the widely studied CoFeB/MgO system, our combined experimental and theoretical studies imply that the Co(Fe)-O-Mg bond plays an important role in the realization of strong PMA in Co(Fe)/oxide heterostructures instead of the widely perceived Co-O bond only.

The remainder of this paper is organized as follows. Section II describes the experimental details. Section III A presents the Co thickness dependence of the effective magnetic anisotropy. In Sec. III B, we present the experimental results of the oxygen and Mg effect on the magnetic anisotropy. The *ab initio* calculation results are presented and discussed in Sec. III C to elucidate the roles of each element in the Co-O-Mg bond, followed by conclusions in Sec. IV.

II. EXPERIMENTAL DETAILS AND THEORETICAL CALCULATIONS

All the samples were deposited on the Si/SiO_2 (300-nm) substrate, which was cut into $2 \times 2\,\text{mm}^2$ squares in order to accommodate the small gap of the electromagnet inside the UHV chamber which provides a perpendicular field up to 2/kOe. In order to avoid a short circuit by Pt deposited on the sample holder, an underlayer of Ta(1.5)/Pt(3) (unless specified otherwise and the number inside the parentheses indicates the thickness in nanometers) was deposited *ex situ* in a dc magnetron sputter with a base pressure of $<4 \times 10^{-8}$ mbar and a process pressure of 4×10^{-3} mbar. After the deposition of Ta/Pt, the sample was immediately loaded into the Omicron UHV system and annealed at 110 °C for 1 h to remove moisture on the surface before subsequent *in situ* deposition and electrical measurements. Details about the UHV system can be found elsewhere [24–26]. Oxygen exposure and AHE measurements were performed in the same chamber. The oxygen exposure was carried out by gradually increasing the partial pressure from the background vacuum to $1 \times 10^{-8} - 3 \times 10^{-7}$ mbar through controlling the duration between 5 and 60 min. The AHE measurements were performed by directly probing the four corners of the sample. The deposition of Co and Mg was performed *in situ* using K cells in the preparation chamber with a rate of 0.033 and $0.265\,\text{Å}\,\text{s}^{-1}$, respectively. As we will discuss shortly, in the Mg dusting experiment in order to minimize the amount of Mg deposited on the Co surface, we heated up the Mg source but kept the shutter closed. Mg dusting of the Co surface was achieved through Mg atoms leaked out from the K cell through the small spacing between the shutter and the cell. There was no exposure to ambient after the sample was loaded into the UHV system and throughout the *in situ* studies.

Density functional theory (DFT) with the projected augmented-wave method was performed by employing the Vienna *ab initio* simulation package [27]. The generalized gradient approximation in the form of Perdew-Burke-Ernzerhof [28] was chosen as an exchange-correlation potential. The electron wave functions were expanded by a plane-wave basis set with a cutoff energy of 500 eV. The Brillouin zone is sampled by a $21 \times 21 \times 1$ k-point mesh, and the convergence criterion of total energy is set to be 10^{-6} eV. In general, the calculation includes three steps. First, full structural optimizations were performed until none of the forces exceeded $0.01\,\text{eV}\,\text{Å}^{-1}$. Next, the Kohn-Sham equations were solved with a collinear calculation without spin-orbit coupling (SOC) to determine the charge distribution of the system ground state. Finally, SOC was taken into account, and the magnetic anisotropy energy (MAE) was calculated as $E_{\text{MAE}} = -\frac{1}{a^2}(E_\perp - E_{||})$, where a is the in-plane lattice constant and $E_\perp$ ($E_{||}$) is the total energy of the system with spins oriented in the out-of-plane (in-plane) direction. As will be discussed shortly, at the Co thickness range investigated, the contribution to effective anisotropy from the bulk magnetocrystalline anisotropy is much smaller than interface anisotropy (K_s), and therefore E_{MAE} can be approximated as equal to K_s in the macrospin model.

III. RESULTS AND DISCUSSION

A. Co thickness dependence of magnetic anisotropy revealed by AHE measurements

In the first round of measurements, t_{Co} was systematically varied to understand how the effective magnetic anisotropy of the Co/Pt bilayer depends on t_{Co}. Figures 1(a)–1(c) show the AHE loops for Ta(1.5)/Pt(3)/Co(t_{Co}) with $t_{\text{Co}} = 0.2 - 1.9$ nm. Due to the large range of sweeping fields needed for samples with different Co thicknesses and for the sake of clarity, we present the results in three separate subplots: (a) $t_{\text{Co}} = 0.2$ and 0.4 nm, (b) $t_{\text{Co}} = 0.6 - 1.7$ nm, and (c) $t_{\text{Co}} = 1.8$ and 1.9 nm. The offset of the AHE raw data was corrected, and the curves are vertically shifted for clarity except for the first curve in each subplot. As can be seen in Fig. 1(a), there is hardly any observable AHE at $t_{\text{Co}} = 0.2$ nm, presumably caused by the nonconformal coverage of Pt by Co at this small thickness. When Co forms discrete islands on Pt, due to the size effect, its crystalline magnetic anisotropy may become too small to support ferromagnetism at room temperature; this may explain why the AHE signal is diminished at $t_{\text{Co}} = 0.2$ nm. With increasing the thickness, the Co islands will grow and coalesce to form large patches, leading to an increase in magnetic anisotropy. As the entire film does not exhibit PMA, the AHE curve has a mixture of characteristics of PMA and in-plane magnetic anisotropy (IMA) films as shown in Fig. 1(a) for $t_{\text{Co}} = 0.4$. When t_{Co} is further increased to 0.6 nm as shown in Fig. 1(b), nearly a square-shaped loop was observed, suggesting the onset of PMA. The squareness of the AHE curves remains almost the same until t_{Co} reaches 1.6 nm, although the coercivity of Co increases significantly from 0.6 to 1.2 nm and then gradually decreases. At $t_{\text{Co}} = 1.7$ nm, part of the film starts to exhibit IMA, which becomes more dominant over PMA when t_{Co} increases to 1.8 and 1.9 nm as shown in Fig. 1(c).

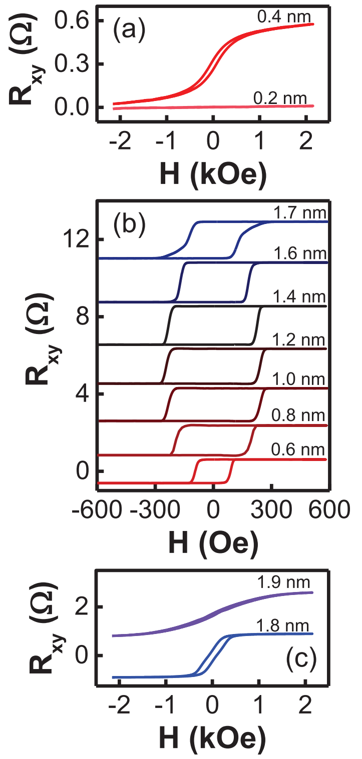

FIG. 1. (a)–(c) AHE loops for Ta(1.5)/Pt(3)/Co(t_{Co}) with $t_{\mathrm{Co}} = 0.2-1.9$ nm. Note that the curves in (a)–(c) are vertically shifted for clarify.

The transition from PMA to IMA in Fig. 1(c) is similar to the typical SRT behavior observed in ultrathin Co or Fe films [22,23]. The transition can be understood as a continuous reorientation of the easy axis from the perpendicular to the in-plane direction via the intermediate "easy cone state" with the easy axis canted from the perpendicular direction [29–31]. Since the field strength of the electromagnet in our UHV chamber is insufficient for quantifying PMA by performing Hall measurements using an in-plane field, we employ the macrospin approximation to gain some insight on PMA through fitting the AHE curves at different Co thicknesses near the SRT region. Following the coordinate notion in Fig. 2(a) and with the applied field in the z direction ($\theta_H = 0$), the free-energy density of the film can be expressed as [29]

$$E = K_{\mathrm{eff}}\sin^2\theta + K_2\sin^4\theta - HM_s\cos\theta, \tag{1}$$

where K_{eff} is the effective anisotropy constant defined phenomenologically as $K_{\mathrm{eff}} = K_1 - 2\pi M_s^2 + K_s/t_{\mathrm{Co}}$ with K_s as the interface anisotropy constant, K_1 and K_2 as the second- and fourth-order magnetocrystalline anisotropy constants, M_s as the saturation magnetization, H as the applied magnetic field, and θ as the angles between the magnetization and the z direction. For every set of K_1, K_2, K_s, and M_s values, the equilibrium magnetization direction $\theta(H,t_{\mathrm{Co}})$ can be obtained numerically through energy minimization from which the AHE curve can be obtained.

Before proceeding to numerical calculations, it is useful to estimate the range of K_1, K_2, and K_s analytically. The energy minimization requires $\frac{\partial E}{\partial \theta} = 0$, which yields

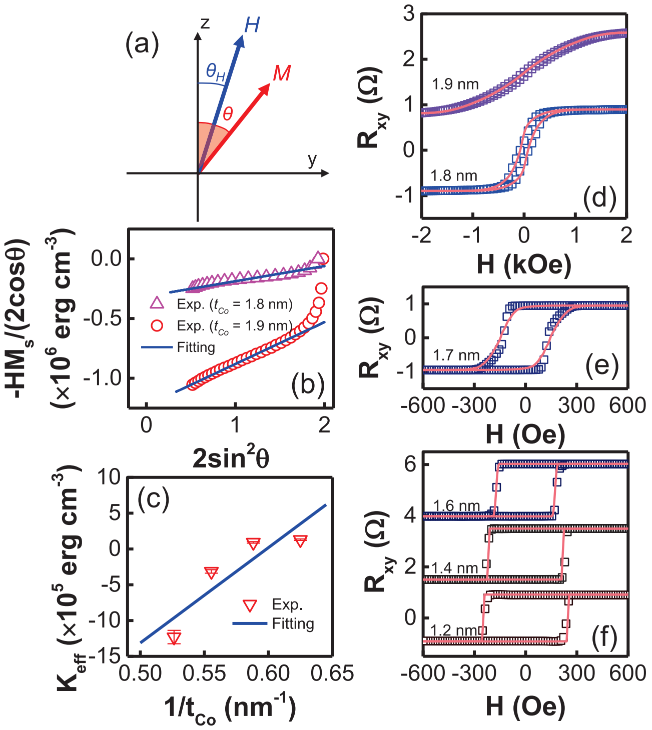

FIG. 2. (a) Schematic of the coordinate system adopted for deriving Eq. (1); (b) plot of $-HM_s/(2\cos\theta)$ against $2\sin^2\theta$ from AHE loops of the $t_{\mathrm{Co}} = 1.9$-nm (circle) and $t_{\mathrm{Co}} = 1.8$-nm (triangle) samples and the linear fitting (solid line); (c) summary of the estimated K_{eff} values with $t_{\mathrm{Co}} = 1.6-1.9$ nm; (d) and (e) fitting of AHE loops for Ta(1.5)/Pt(3)/Co(t_{Co}) with $t_{\mathrm{Co}} = 1.7-1.9$ nm using the normal distribution; (f) fitting of the AHE loops with $t_{\mathrm{Co}} = 1.2-1.6$ nm without consideration of the normal distribution (open square: experimental data; solid line: fitting results). Note that the curves in (d)–(f) are vertically shifted for clarify.

$$2\sin 2\theta\left(K_{\mathrm{eff}} + 2K_2\sin^2\theta + \frac{HM_s}{2\cos\theta}\right) = 0. \tag{2}$$

Equation (2) has two sets of solutions. By correlating the experimental data in Figs. 1(a)–1(c) with the three anisotropy cases discussed in the Appendix, it can be identified that the slanted loops at $t_{\mathrm{Co}} = 1.8$ and 1.9 nm are associated with the solutions of $K_{\mathrm{eff}} + 2K_2\sin^2\theta + \frac{HM_s}{2\cos\theta} = 0$, whereas the relatively square loops at $t_{\mathrm{Co}} = 1.6$ and 1.7 nm come from the solution of $2\sin 2\theta = 0$. For the former case, we further plotted $-HM_s/(2\cos\theta)$ against $2\sin^2\theta$ with $M_s = 1407$ emu cm^{-3} for the two samples in Fig. 2(b). In the plot, $\cos\theta$ is calculated by normalizing R_{xy} at each H, and only the data from the reversible portion below the saturation field is used. In this way, K_{eff} and K_2 at $t_{\mathrm{Co}} = 1.8$ and 1.9 nm can be estimated by a linear fitting. For the latter case, the magnetization switches at $H = \pm\frac{2K_{\mathrm{eff}}}{M_s}$; therefore, K_{eff} at $t_{\mathrm{Co}} = 1.6, 1.7$ nm can be obtained from the H_c of the AHE curve. In Fig. 2(c), K_{eff} values at different thicknesses are plotted against $1/t_{\mathrm{Co}}$. Through linear fitting, K_1 and K_s are estimated as 4.47×10^6 erg cm^{-3} and 1.33 erg cm^{-2}, respectively.

TABLE I. Summary of the fitting parameters of the AHE loops in the range of $t_{\rm Co} = 1.2-1.9$ nm using Eq. (1), and N. A. represents not available.

$t_{\rm Co}$ (nm)	K_1 (erg cm^{-3})	K_2(erg cm^{-3})	K_s (erg cm^{-2})	σ (nm)
1.9	4.37×10^6	1.25×10^5	1.33	0.063
1.8	4.85×10^6	1.20×10^5	1.33	0.060
1.7	4.60×10^6	1.35×10^5	1.33	0.017
1.6	4.25×10^6	1.20×10^5	1.33	N. A.
1.4	3.09×10^6	1.20×10^5	1.33	N. A.
1.2	1.53×10^6	1.20×10^5	1.33	N. A.

We now turn to numerical minimization of Eq. (1) by using the obtained K_1, K_2, and K_s as the starting values. Due to the sensitivity of AHE curves to thickness at around the SRT critical thickness, it is difficult to fit the curves by assuming a uniform $t_{\rm Co}$ across the entire sample. In reality, it is very likely that the sample consists of a mixture of PMA, easy cone, and IMA states due to subtle thickness variation over a relatively large size sample. To account for the thickness effect, we assumed that the sample consists of areas with different Co thicknesses and the partial area of the film at thickness $t_{\rm Co}$ follows a normal distribution $f(t_{\rm Co},\bar{t}_{\rm Co}) = \frac{1}{\sqrt{2\sigma^2\pi}}\exp[-\frac{(t_{\rm Co}-\bar{t}_{\rm Co})^2}{2\sigma^2}]$ with $\bar{t}_{\rm Co}$ as the average thickness, σ as the standard deviation, and $t_{\rm Co}$ taken in the range of $0-2\bar{t}_{\rm Co}$. With this assumption the AHE loop at $\bar{t}_{\rm Co}$ is calculated as $R_{xy}(H,\bar{t}_{\rm Co}) = \int_0^{2\bar{t}_{\rm Co}} f(t_{\rm Co},\bar{t}_{\rm Co})\cos\theta(H,t_{\rm Co})dt_{\rm Co}$. The integration is performed numerically by dividing the Co thickness in the range of $0-2\bar{t}_{\rm Co}$ in 1001 steps. As shown in Figs. 2(d) and 2(e), by fitting the AHE loops at $t_{\rm Co} = 1.7-1.9$ nm (average nominal thickness of Co), we obtained $K_1 = (4.52 \pm 0.33) \times 10^6$, $K_2 = (1.27 \pm 0.08) \times 10^5$erg cm^{-3}, and $K_s = 1.33$ erg cm^{-2}. These results imply that at the present $t_{\rm Co}$ range, $K_{\rm eff}$ is dominated by the $K_s/t_{\rm Co}$ term and the magnitude of K_s is comparable to the value reported in Pt/Co multilayers (around $0.20-1.15$ erg cm^{-2}) [32] and that in Pt/Co/AlO$_x$ heterostructures (around $0.64-1.74$ erg cm^{-2}, calculated using the bulk K_1 value) [6,7]. On the other hand, for the $t_{\rm Co} = 1.2-1.6$-nm samples as shown in Fig. 2(f), the AHE loops can be fitted without the additional consideration of thickness distribution. The reason for this is that below the critical thickness of around 1.7 nm, despite thickness variations, the entire sample is mostly in the PMA state, and thus the AHE loops remain square shaped. Table I summarizes the parameters used for the fitting of samples with $t_{\rm Co} = 1.2-1.9$ nm. It should be noted that the K_1, K_2, K_s values remain almost the same for $t_{\rm Co} = 1.6-1.9$ nm, whereas a much smaller K_1 is needed for $t_{\rm Co} = 1.2-1.4$ nm. When $t_{\rm Co}$ is below 1.0 nm, the AHE loops can only be reproduced by using a negative K_1 (not shown here), which contradicts the assumption of $K_1 > 0$. In fact, these results can be anticipated from the limitation of the macrospin model for samples at PMA states, especially with very small thicknesses. Nevertheless, it is safe to say that the model is suitable to account for most of the experimental observations near the SRT thickness region.

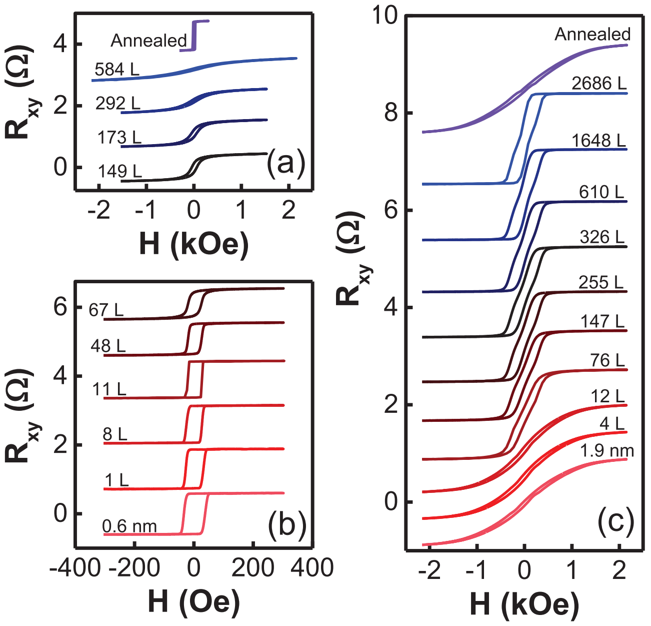

FIG. 3. (a) and (b) AHE loops for Ta(1.5)/Pt(3)/Co(0.6) with different oxygen preexposure doses; (c) AHE loops for Ta(1.5)/Pt(3)/Co(1.9) with different oxygen preexposure doses. The topmost curves in (a) and (c) are obtained after annealing. Note that the curves in (a)–(c) are shifted vertically for clarity.

B. Oxygen exposure and Mg dusting effect on magnetic anisotropy

Next we present the oxygen effect on the magnetic anisotropy of Pt/Co bilayers. Figures 3(a) and 3(b) show the AHE loops for another sample with a structure of Ta(1.5)/Pt(3)/Co(0.6) at different oxygen exposure doses (here L is the Langmuir unit with one langmuir corresponding to an exposure of 1.33×10^{-6} mbar for 1 s). A full coverage of the energy favorable fcc hollow sites on the hcp Co surface (to be discussed later) thus requires an oxygen exposure dose of about 5.2 L, assuming a unity sticking coefficient. Again all the curves but the lowest one (without O exposure) are vertically shifted. As can be seen, both the coercive field and the AHE signal decrease as the dose increases, both of which are signatures of the gradual transition from PMA to IMA. Moreover, as shown in Fig. 3(a), the exposed sample can return to the original PMA state after a mild annealing at 110 °C for 1 h in UHV. At this stage, one may be tempted to associate the transition with an O exposure-induced decrease in K_s, which is indeed the case as revealed by *ab initio* calculations (to be discussed later) for the ultrathin Co layer. However, as shown in Fig. 3(c) for a thicker sample with the structure of Ta(1.5)/Pt(3)/Co(1.9), upon O exposure, both the coercive field and the AHE signal show the opposite trend, i.e., the transition from IMA to PMA. Similarly, the AHE loop recovers after a mild annealing. The different oxygen dose dependences in Fig. 3 for the two samples suggest at least that the oxygen exposure effect cannot be explained by the change in K_s alone. Instead, the behavior of both samples can be explained reasonably well by taking into additional consideration that the oxygen exposure seems to induce an

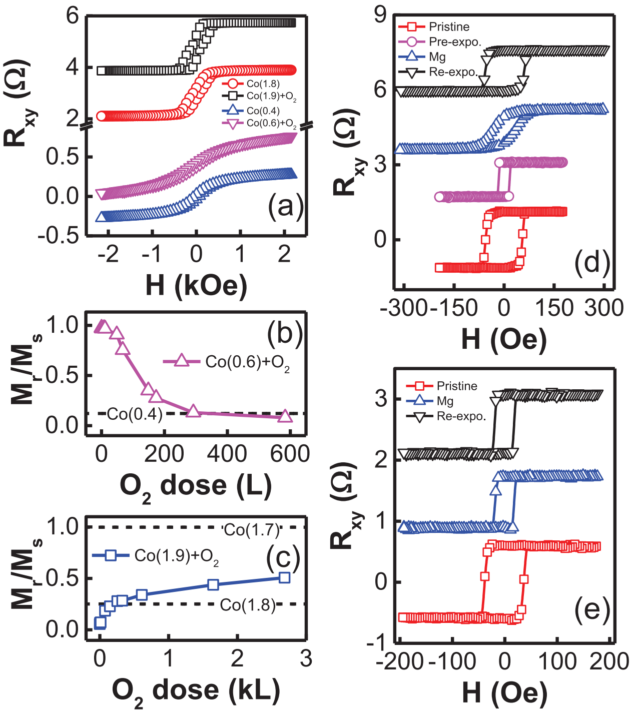

FIG. 4. (a) Comparison of the AHE loops for pristine samples with $t_{\mathrm{Co}} = 0.4$ and 1.8 nm and O exposed samples with $t_{\mathrm{Co}} = 0.6$ and $t_{\mathrm{Co}} = 1.9$ nm; (b) oxygen dose dependence of the M_r/M_s ratio for the $t_{\mathrm{Co}} = 0.6$-nm sample; (c) oxygen dose dependence of the M_r/M_s ratio for the $t_{\mathrm{Co}} = 1.9$-nm sample; (d) comparison of the AHE loops for Ta(1.5)/Pt(3)/Co(0.8) at pristine, preexposed, Mg dusting, and reexposed states; (e) comparison of the AHE loops for Ta(1.5)/Pt(3)/Co(0.6) at pristine, Mg dusting, and reexposed states. Note that the M_r/M_s ratio of the $t_{\mathrm{Co}} = 0.4$, 1.7, 1.8-nm pristine samples is added in (b) and (c) as a reference, and the curves in (a), (d), and (e) are shifted vertically for clarity.

effect which corresponds to an effective reduction in t_{Co}. To shed more light on this point, Fig. 4(a) compares the AHE loops for two sets of samples: (i) a pristine sample with $t_{\mathrm{Co}} = 0.4$ nm and an O exposed sample with $t_{\mathrm{Co}} = 0.6$ nm and (ii) a pristine sample with $t_{\mathrm{Co}} = 1.8$ nm and an O exposed sample with $t_{\mathrm{Co}} = 1.9$ nm. The similarity of the AHE loops in both sets of samples agrees with the above hypothesis, i.e., upon O exposure, the effective Co thickness decreases. In fact, it has been reported earlier that the oxygen exposure of transition FMs can cause the partial or complete quenching of magnetism due to the chemisorption of oxygen, the formation of oxides, or both [33,34]. For a more quantitative understanding of the present case, the remanent-magnetization-(M_r)-to-M_s ratio is extracted from AHE loops at different thicknesses and oxygen doses by assuming $M_r/M_s = R_{xy}(0)/R_{xy}(H_{\max})$, where $R_{xy}(0)$, $R_{xy}(H_{\max})$ is the Hall resistance at a zero field and a maximum field, respectively. Figures 4(b) and 4(c) summarize the ratios at different oxygen doses for the $t_{\mathrm{Co}} = 0.6$-nm exposed sample and the $t_{\mathrm{Co}} = 1.9$-nm exposed sample, respectively. In addition, the ratios of the $t_{\mathrm{Co}} = 0.4, 1.7, 1.8$-nm pristine samples are added in the figures as references. By comparing these results, it can be estimated that the O exposure-induced Co thickness reduction is around 0.1–0.2 nm under the present exposure conditions. This together with the observation of the recovery of K_{eff} after mild annealing elucidates the main picture of O exposure, i.e., the moment of the topmost Co layer is largely quenched by oxygen adsorption at the Co surface, which in turn induces either PMA → IMA or IMA → PMA transition at small or large Co thickness, respectively. Similar trends were also observed in a few more samples with different t_{Co} values (not shown here). It should be noted that based on the experimental data presented so far, the contribution of a Co-O interface to overall K_s including the Pt-Co interface cannot be quantified because its effect is masked out by the more dominant change caused by t_{Co}.

The aforementioned dependence of PMA on the O dose and the decrease in effective t_{Co} upon O exposure are apparently different from the situation in Pt/Co/AlO$_x$ heterostructures [6,7] where a maximum PMA usually is obtained upon oxidation under optimal conditions. This naturally leads to the question about the role of the M-O bond in promoting the PMA. To elucidate the role of M in the M-O bond, two more sets of experiments were carried out by using Mg as the dusting layer. It should be noted that a relatively thick layer of Mg (∼0.8 nm) would lead to IMA of Co regardless of whether the Co surface is oxygen exposed or not. If we had used the precalibrated deposition rate of 0.265 Å s^{-1}, the shutter could only be opened for a few seconds, which would make it difficult to achieve a precise control of the amount of Mg deposited on the Co surface due to manual operation of the shutter. Therefore, in the Mg dusting experiment, we heated up the K cell to have a nominal deposition rate of 0.265 Å s^{-1} but with the K-cell shutter closed during deposition. In the first series of experiments, Mg was dusted on O preexposed samples and subsequently exposed the Mg dusted samples to oxygen again (hereafter we refer it as the "reexposed" sample). As an example, Fig. 4(d) compares the AHE loops for the sample of Ta(1.5)/Pt(3)/Co(0.8) at different stages including pristine, O preexposed (a dose of 1218 L), Mg dusted, and O reexposed (a dose of 3760-L) states. As can be seen, after Mg dusting and O reexposure, the sample is almost recovered back to the pristine state. In some other samples (not shown here), PMA was recovered after Mg dusting without further reexposure to oxygen, which is probably due to the variation in the amount of adsorbed oxygen and/or Mg adatoms in the preexposure and/or dusting process among different samples. On the other hand, as shown in Fig. 4(e), direct Mg dusting on a pristine Ta(1.5)/Pt(3)/Co(0.6) sample slightly weakens the PMA, and reexposure to oxygen (a dose of 3548 L) has little effect on it. Since oxygen mainly affects the surface layer, the presence of a Mg layer largely protects the Co layer from interacting with oxygen. The weakening of PMA in this case therefore mostly results from the Co-Mg bond. Both observations in Figs. 4(d) and 4(e) suggest that Mg in MgO indeed plays an active role in Pt/Co/MgO heterostructures.

C. *Ab initio* calculations of oxygen adsorption and Mg dusting effect

To shed light on the respective roles of each element in the Co-O-Mg bond, first-principles calculations are carried out. The pristine Pt/Co is explored first as a reference. The

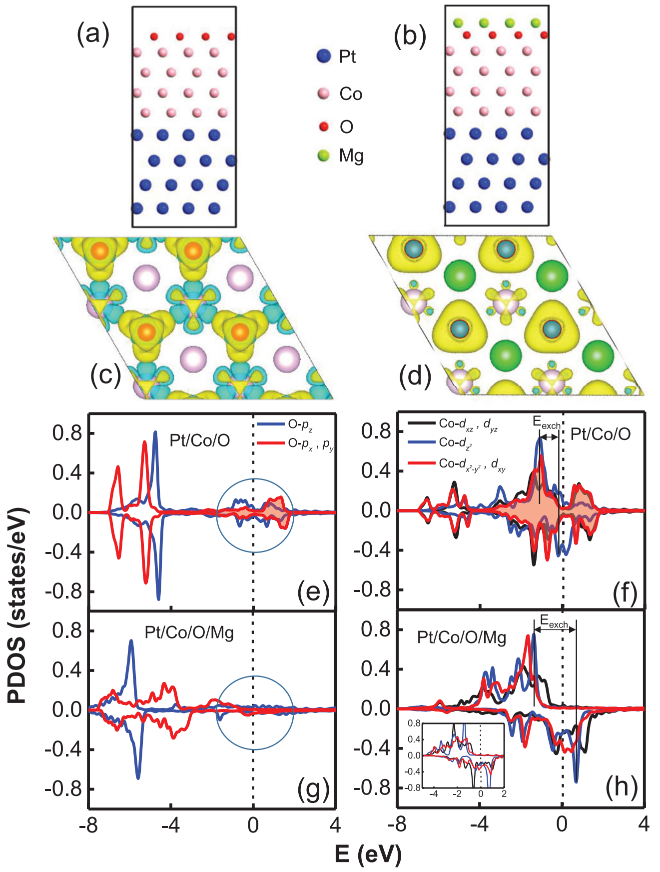

FIG. 5. Schematics for optimized structures used in *ab initio* calculations of (a) oxygen-exposed Pt/Co/O; (b) Mg dusted pre-exposed Pt/Co/O/Mg. Note that Pt, Co, O, and Mg are represented by blue, pink, red, and green balls, respectively. The charge-density difference (top view) plotted using an isovalue of $0.012\,e\,\text{Å}^{-3}$ for (c) Pt/Co/O and (d) Pt/Co/O/Mg. The red (blue) region indicates an accumulation (depletion) of electrons. Majority spin (positive) and minority spin (negative) PDOS on the p orbitals of O and d orbitals of Co in (e) and (f) for Pt/Co/O and in (g) and (h) for Pt/Co/O/Mg, respectively. The zero of energy is set at the Fermi level, and a dashed line is added as a guidance to the eye. The inset in (h) is PDOS on the d orbitals of Co in Pt/Co.

TABLE II. Summary of *ab initio* calculated m_S, m_L, and K_s for the optimized structures of Pt/Co, Pt/Co/O, Pt/Co/O/Mg, respectively.

Structure		Moment (μ_B per atom)				K_s (erg cm^{-2})
		Co$_1$	Co$_2$	Co$_3$	Co$_4$	
Pt/Co	m_S	1.83	1.72	1.74	1.82	0.71
	m_L	0.10	0.11	0.11	0.13	
Pt/Co/O	m_S	1.80	1.72	1.73	0.27	0.36
	m_L	0.10	0.11	0.13	0.01	
Pt/Co/O/Mg	m_S	1.82	1.72	1.69	1.92	0.70
	m_L	0.10	0.11	0.12	0.13	

schematics of the optimized structures after oxygen exposure (Pt/Co/O) and Mg dusting (Pt/Co/O/Mg) are shown in Figs. 5(a) and 5(b), respectively. Previous studies report that O atoms not O molecules are chemisorbed at a low dose upon exposure of the Co surface because the strong surface interaction can break the O-O bond [35–38]. Our total-energy calculations suggest both adsorbed O and Mg favor the fcc hollow sites on the Co surface, which is consistent with low-energy electron-diffraction studies [39,40] and DFT calculations [41,42]. Table II summarizes the calculated spin moments (m_S), orbital moments (m_L), and K_s for all the structures with geometry optimization. Notably, the spin moment (m_S) of the topmost Co layer decreases from 1.82 μ_B per atom to 0.27 μ_B per atom upon O adsorption and recovers to 1.92 μ_B per atom after adding Mg adatoms. This variation of magnetic moments for the topmost Co atom (from unpaired electrons) is directly correlated to the induced change in the charge distribution in the two structures. For a clear view of the charge-transfer effect, we depict the charge-density difference in Fig. 5(c) for Pt/Co/O and in Fig. 5(d) for Pt/Co/O/Mg. As can be seen from the color [see the caption of Fig. 5], in Pt/Co/O, the charge transfers from the topmost Co to O atoms due to the high electronegativity of the O atom. Whereas in Pt/Co/O/Mg, O atoms gain electrons directly from Mg atoms, and this in turn results in the transferring of electrons back to Co atoms. More quantitatively, Bader charge analysis shows that the topmost Co layer transfers 0.84e per atom to the O atom in Pt/Co/O, and this electron loss is compensated by Mg with 0.40e per atom transferring back to Co in Pt/Co/O/Mg. In addition, the orbital moment (m_L) of Co layers follows the same trend as m_S, resulting in the variation of K_s [43–46]. It decreases from 0.71 to 0.36 erg cm^{-2} in Pt/Co/O and returns to 0.70 erg cm^{-2} in Pt/Co/O/Mg. All these calculation results are in qualitative agreement with the experimental ones, although in the experimental case, it is difficult to separate the contribution to effective anisotropy by K_s and the demagnetizing energy.

To have a better understanding of the physical origin of the changes in m_S and K_s, the projected densities of the states (PDOS) of d orbitals of the topmost Co layer and p orbitals of the O atom are plotted for the cases of Pt/Co/O [Figs. 5(e) and 5(f)] and Pt/Co/O/Mg [Figs. 5(g) and 5(h)]. The PDOS of the reference (Pt/Co) is inserted in Fig. 5(h) for comparison. As can be seen, the exchange splitting energy (E_{exch}) in Fig. 5(f) (0.85 eV) is much smaller than that in Fig. 5(h) (2.03 eV) and the inset of Fig. 5(h) (2.13 eV), resulting in a reduced value of m_S in Pt/Co/O compared with Pt/Co/O/Mg and Pt/Co. On the other hand, the change in PMA can be understood from the second-order perturbation theory in which K_s is expressed as [47,48]

$$K_s \propto \xi^2 \sum_k \sum_{o,u} \frac{|\langle k_o|L_z|k_u\rangle|^2 - |\langle k_o|L_x|k_u\rangle|^2}{\varepsilon_{k_u} - \varepsilon_{k_o}}, \tag{3}$$

where ξ is an average of the spin-orbit-coupling (SOC) coefficient, k_o and k_u are the occupied and unoccupied states with the wave-vector k, L_z and L_x are the angular momentum operators along the z and x directions, respectively, and ε_{k_u} and ε_{k_o} are the energies of the occupied and unoccupied states, respectively. As can be seen from Eq. (3), the SOC between the occupied and the unoccupied states with the same magnetic quantum number (m) through the L_z operator enhances K_s, whereas that with different m values through the L_x operator weakens it. From the PDOS in Fig. 5, we can find that O-p_x and O-p_y ($m = \pm 1$) are degenerate and five d states can be subdivided into Δ_1 (d_{z^2})($m = 0$), Δ_3 (d_{xz}, d_{yz})($m = \pm 1$), and Δ_4 ($d_{x^2\text{-}y^2}$, d_{xy})($m = \pm 2$) groups. Figures 5(e) and 5(f) show the hybridization between p states of the O atom and d states of the Co atom for both occupied and unoccupied states near the Fermi level. Based on Eq. (3), two hybridizations $\langle p_x|L_x|d_{x^2\text{-}y^2}\rangle$ and $\langle p_x|L_x|d_{xy}\rangle$ contribute negatively to the PMA, favoring in-plane anisotropy, whereas only one orbital hybridization $\langle p_z|L_z|d_{z^2}\rangle$ contributes positively to PMA. Overall, the adsorbed O leads to the decrease in K_s. This is consistent with our experimental result ($t_{\mathrm{Co}} =$ 0.6 nm) and the previous experimental report that a negative contribution from the Co-O interface (hollow sites) $K_s^{\text{Co-O}} = -0.04\,\text{erg cm}^{-2}$ was experimentally extracted on hydroxide modified Au(111)/Co surfaces [49]. After depositing Mg, Fig. 5(h) shows that O states near the Fermi level are significantly reduced, resulting in the recovery of K_s. We did not observe a notable enhancement of PMA in the Co-O-Mg interfaces as compared to Pt/Co, which is presumably caused by the fact that, in this case, the PMA from Pt-Co is more dominant.

IV. CONCLUSIONS

To summarize, we have performed an anatomical study of the O and Mg effect on the magnetic anisotropy of Pt/Co bilayers using *in situ* AHE measurements. It was found that the oxygen adsorption affects the effective magnetic thickness of Co and thereby changes its magnetic anisotropy. The subsequent Mg dusting can recover the magnetic moment as well as the magnetic anisotropy. *Ab initio* calculations unveil the underlying physics of the change in the magnetic moment and interfacial PMA. Our results suggest that the role of the Co-*M*-O bond in the realization of PMA at (Co)Fe/*M*O$_x$ interfaces may have been overlooked in previous studies relative to the Co(Fe)-O bond. Our paper may stimulate further studies on this important interface by adopting a more holistic approach.

ACKNOWLEDGMENTS

The authors thank Z. Luo for her help with the sample preparation and Dr. X. Qin for her help with the discussions and calculations. Y.W. would like to acknowledge support from the Ministry of Education, Singapore under its Tier 2 Grant (Grant No. MOE2013-T2-2-096) and the Singapore National Research Foundation, Prime Minister's Office under its Competitive Research Programme (Grant No. NRF-CRP10-2012-03). L.S. would like to acknowledge support from the ACRF Tier 1 Research Project (Project No. R-144-000-361-112). Y.W., Y.F., and L.S. are members of the Singapore Spintronics Consortium (SG-SPIN).

APPENDIX: MACROSPIN MODEL OF BILAYER

The Pt/Co bilayer can be treated phenomenologically using the macrospin model in which the magnetization vector $\boldsymbol{M}$ is assumed to be uniform over the film and coherently rotated upon sweeping the external magnetic field. The free-energy density consists of dipolar (E_d), magnetocrystalline (E_{mc}), interface (E_S), and Zeeman (E_Z) energies, respectively, whose expressions are given below [29],

$$E_d = -2\pi M_s^2 \sin^2\theta, \tag{A1}$$

$$E_{mc} = K_1 \sin^2\theta + K_2 \sin^4\theta, \tag{A2}$$

$$E_s = K_s \sin^2\theta / t_{\mathrm{Co}}, \tag{A3}$$

$$E_z = -HM_s\cos\theta, \tag{A4}$$

where K_s is the interface anisotropy constant, K_1 and K_2 are the second- and fourth-order magnetocrystalline anisotropy constants, respectively, M_s is the saturation magnetization, H is the applied magnetic field, t_{Co} is the Co thickness, and θ is the angle between the magnetization and the z direction. We assume that $K_1, K_2, K_s > 0$ and are all independent of t_{Co}. To determine the equilibrium state of $\boldsymbol{M}$ at a specific H value, numerical energy minimization is performed on the total energy density,

$$\begin{aligned} E &= -2\pi M_s^2 \sin^2\theta + K_1 \sin^2\theta + K_2 \sin^4\theta \\ &\quad + K_s \sin^2\theta / t_{\mathrm{Co}} - HM_s\cos\theta. \end{aligned} \tag{A5}$$

Before proceeding with the simulations as presented in Sec. III A, we first take a look at all the anisotropy energy terms to have a better understanding of the macrospin model. For easy treatment, the effective anisotropy K_{eff} is defined phenomenologically as $K_{\mathrm{eff}} = K_1 - 2\pi M_s^2 + K_s/t_{\mathrm{Co}}$. In this way, the effective anisotropy energy including E_{mc}, E_d, and E_s can be rewritten as

$$E_K = K_{\mathrm{eff}} \sin^2\theta + K_2 \sin^4\theta. \tag{A6}$$

Equation (A6) can be rearranged further in the form of

$$E_K = K_2\left[(\sin^2\theta) + \frac{K_{\mathrm{eff}}}{2K_2}\right]^2 - \frac{K_{\mathrm{eff}}^2}{4K_2}. \tag{A7}$$

Equation (A7) is a special case of Eq. (A5) with $H = 0$, which corresponds to the remanent state of $\mathbf{M}$. Three different equilibrium states can be inferred from Eq. (A7) depending on the values of K_{eff} and K_2, which are summarized as follows:

(1) $K_{\mathrm{eff}} < -2K_2$

In this case, a minimum of $E_K = K_{\mathrm{eff}} + K_2$ is obtained at $\theta = \pm\pi/2$. This suggests that, in the present case, $\boldsymbol{M}$ lies in plane at remanence. Since K_1, K_2, and K_s are positive constants (based on our earlier assumption) for $K_{\mathrm{eff}} = K_1 - 2\pi M_s^2 + K_s/t_{\mathrm{Co}}$ to be negative, it requires a large t_{Co}. This explains our experimental observations that at large t_{Co}, the Pt/Co bilayer favors IMA.

(2) $-2K_2 \leqslant K_{\mathrm{eff}} \leqslant 0$

E_K has a minimum of $-\frac{K_{\mathrm{eff}}^2}{4K_2}$ at $\theta = \arcsin(\sqrt{-\frac{K_{\mathrm{eff}}}{2K_2}})$ or $\pi - \arcsin(\sqrt{-\frac{K_{\mathrm{eff}}}{2K_2}})$. This means that the remanent $\boldsymbol{M}$ is at an inclined angle with respect to the z direction. Such a kind of state has been observed experimentally in PMA films within a specific range of film thickness and is often referred to as a cone state in macrospin approximation.

(3) $K_{\mathrm{eff}} > 0$

The minimum of E_K is obtained at $\theta = 0,\pi$ with a magnitude of 0. This condition is satisfied at small t_{Co} where stable perpendicular PMA is achieved in the system.

Based on the above discussion of Eq. (A5), it is clear that with increasing t_{Co}, the Co/Pt bilayer experiences a transition from PMA to IMA via the intermedium cone state. This transition often is referred to as the SRT, which is widely observed in ultrathin Fe, Ni, and Co films [21–23]. Moreover, at the critical thickness of the SRT, the remanence can serve as a good indicator for the anisotropy state.

---

[1] J.-G. Zhu and C. Park, Mater. Today **9**, 36 (2006).
[2] A. Brataas, A. D. Kent, and H. Ohno, Nature Mater. **11**, 372 (2012).
[3] S. Ikeda, K. Miura, H. Yamamoto, K. Mizunuma, H. D. Gan, M. Endo, S. Kanai, J. Hayakawa, F. Matsukura, and H. Ohno, Nature Mater. **9**, 721 (2010).
[4] D. C. Worledge, G. Hu, D. W. Abraham, J. Z. Sun, P. L. Trouilloud, J. Nowak, S. Brown, M. C. Gaidis, E. J. O'Sullivan, and R. P. Robertazzi, Appl. Phys. Lett. **98**, 022501 (2011).
[5] D. Lacour, M. Hehn, M. Alnot, F. Montaigne, F. Greullet, G. Lengaigne, O. Lenoble, S. Robert, and A. Schuhl, Appl. Phys. Lett. **90**, 192506 (2007).
[6] A. Manchon, C. Ducruet, L. Lombard, S. Auffret, B. Rodmacq, B. Dieny, S. Pizzini, J. Vogel, V. Uhlir, M. Hochstrasser, and G. Panaccione, J. Appl. Phys. **104**, 043914 (2008).
[7] B. Rodmacq, A. Manchon, C. Ducruet, S. Auffret, and B. Dieny, Phys. Rev. B **79**, 024423 (2009).
[8] H. Garad, L. Ortega, A. Y. Ramos, Y. Joly, F. Fettar, S. Auffret, B. Rodmacq, B. Diény, O. Proux, and A. I. Erko, J. Appl. Phys. **114**, 053508 (2013).
[9] X. Chen, C. Feng, Z. Long Wu, F. Yang, Y. Liu, S. Jiang, M. Hua Li, and G. Hua Yu, Appl. Phys. Lett. **104**, 052413 (2014).
[10] M. Kim, S. Kim, J. Ko, and J. Hong, Appl. Phys. Lett. **106**, 102404 (2015).
[11] A. E. T. Kuiper, M. F. Gillies, V. Kottler, G. W. 't Hooft, J. G. M. van Berkum, C. van der Marel, Y. Tamminga, and J. H. M. Snijders, J. Appl. Phys. **89**, 1965 (2001).
[12] B. Rodmacq, S. Auffret, B. Dieny, S. Monso, and P. Boyer, J. Appl. Phys. **93**, 7513 (2003).
[13] N. D. Telling, G. van der Laan, S. Ladak, and R. J. Hicken, Appl. Phys. Lett. **85**, 3803 (2004).
[14] L. E. Nistor, B. Rodmacq, S. Auffret, and B. Dieny, Appl. Phys. Lett. **94**, 012512 (2009).
[15] A. Hallal, H. X. Yang, B. Dieny, and M. Chshiev, Phys. Rev. B **88**, 184423 (2013).
[16] X. Ou, H. Wang, F. Fan, Z. Li, and H. Wu, Phys. Rev. Lett. **115**, 257201 (2015).
[17] H. X. Yang, M. Chshiev, B. Dieny, J. H. Lee, A. Manchon, and K. H. Shin, Phys. Rev. B **84**, 054401 (2011).
[18] Z. Wang, M. Saito, K. P. McKenna, S. Fukami, H. Sato, S. Ikeda, H. Ohno, and Y. Ikuhara, Nano Lett. **16**, 1530 (2016).
[19] I. G. Rau, S. Baumann, S. Rusponi, F. Donati, S. Stepanow, L. Gragnaniello, J. Dreiser, C. Piamonteze, F. Nolting, S. Gangopadhyay, O. R. Albertini, R. M. Macfarlane, C. P. Lutz, B. A. Jones, P. Gambardella, A. J. Heinrich, and H. Brune, Science **344**, 988 (2014).
[20] T. Hirai, T. Koyama, A. Obinata, Y. Hibino, K. Miwa, S. Ono, M. Kohda, and D. Chiba, Appl. Phys. Express **9**, 063007 (2016).
[21] R. Vollmer, T. Gutjahr-Loser, J. Kirschner, S. van Dijken, and B. Poelsema, Phys. Rev. B **60**, 6277 (1999).
[22] J.-W. Lee, J.-R. Jeong, S.-C. Shin, J. Kim, and S.-K. Kim, Phys. Rev. B **66**, 172409 (2002).
[23] I. G. Baek, H. G. Lee, H. J. Kim, and E. Vescovo, Phys. Rev. B **67**, 075401 (2003).
[24] Y. Wang, Y. Yang, Z. Zhao, C. Zhang, and Y. H. Wu, Appl. Phys. Lett. **103**, 033115 (2013).
[25] Y. Wang, Y. Yang, and Y. H. Wu, J. Vac. Sci. Technol., B: Nanotechnol. Microelectron.: Mater., Process., Meas., Phenom. **32**, 051803 (2014).
[26] L. Qi, Y. Wang, L. Shen, and Y. H. Wu, Appl. Phys. Lett. **108**, 063103 (2016).
[27] G. Kresse and J. Furthmüller, Comput. Mater. Sci. **6**, 15 (1996).
[28] J. P. Perdew, K. Burke, and M. Ernzerhof, Phys. Rev. Lett. **77**, 3865 (1996).
[29] L. Cagnon, T. Devolder, R. Cortes, A. Morrone, J. E. Schmidt, C. Chappert, and P. Allongue, Phys. Rev. B **63**, 104419 (2001).
[30] H. Stillrich, C. Menk, R. Fromter, and H. P. Oepen, J. Appl. Phys. **105**, 07C308 (2009).
[31] K.-W. Park, J.-Y. Park, S.-h. C. Baek, D.-H. Kim, S.-M. Seo, S.-W. Chung, and B.-G. Park, Appl. Phys. Lett. **109**, 012405 (2016).
[32] M. T. Johnson, P. J. H. Bloemen, F. J. A. den Broeder, and J. J. de Vries, Rep. Prog. Phys. **59**, 1409 (1996).
[33] J. Chen, M. Drakaki, and J. L. Erskine, Phys. Rev. B **45**, 3636 (1992).
[34] M. Farle, Surf. Sci. **575**, 1 (2005).
[35] N.-L. Wang, U. Kaiser, O. Ganschow, L. Wiedmann, and A. Benninghoven, Surf. Sci. **124**, 51 (1983).
[36] T. Matsuyama and A. Ignatiev, Surf. Sci. **102**, 18 (1981).
[37] A. Bogen and J. Kuppers, Surf. Sci. **134**, 223 (1983).
[38] G. R. Castro and J. Kippers, Surf. Sci. **123**, 456 (1982).
[39] M. Gierer, H. Over, P. Rech, E. Schwarz, and K. Christmann, Surf. Sci. **370**, L201 (1997).
[40] M. Maglietta, E. Zanazzi, U. Bardi, F. Jona, D. W. Jepsen, and P. M. Marcus, Surf. Sci. **77**, 101 (1978).
[41] S. H. Ma, Z. Y. Jiao, T. X. Wang, and X. Q. Dai, Surf. Sci. **619**, 90 (2014).
[42] S. H. Ma, Z. Y. Jiao, T. X. Wang, and X. Q. Dai, Eur. Phys. J. B **88**, 4 (2015).
[43] A. Al-Zubi, G. Bihlmayer, and S. Blügel, Phys. Rev. B **83**, 024407 (2011).
[44] P. V. Ong, N. Kioussis, P. K. Amiri, J. G. Alzate, K. L. Wang, G. P. Carman, J. Hu, and R. Wu, Phys. Rev. B **89**, 094422 (2014).
[45] C.-G. Duan, J. P. Velev, R. F. Sabirianov, Z. Zhu, J. Chu, S. S. Jaswal, and E. Y. Tsymbal, Phys. Rev. Lett. **101**, 137201 (2008).
[46] M. Callsen, V. Caciuc, N. Kiselev, N. Atodiresei, and S. Blügel, Phys. Rev. Lett. **111**, 106805 (2013).
[47] Z. Bai, L. Shen, Y. Cai, Q. Wu, M. Zeng, G. Han, and Y. P. Feng, New J. Phys. **16**, 103033 (2014).
[48] J. Hu and R. Wu, Phys. Rev. Lett. **110**, 097202 (2013).
[49] N. Di, J. Kubal, Z. Zeng, J. Greeley, F. Maroun, and P. Allongue, Appl. Phys. Lett. **106**, 122405 (2015).